ÓPTICA PURA Y APLICADA
www.sedoptica.es

Type: RESEARCH PAPER
Section: Optoelectronics

Lithographic mask defects mitigation on a multimode interference structure

Mitigación de defectos de la máscara litográfica en una estructura de interferencia multimodo

P. Lourenço[2,3*], A. Fantoni[1,3], J. Costa[1,3], M. Vieira[1,2,3]

1. ISEL/ADEETC - Instituto Superior de Engenharia de Lisboa, Instituto Politécnico de Lisboa, Área Departamental de Engenharia Eletrónica e Telecomunicações e de Computadores, Rua Conselheiro Emídio Navarro, 1, 1959-007 Lisboa, Portugal;

2. Faculdade de Ciências e Tecnologia, FCT, Universidade Nova de Lisboa, Departamento de Engenharia Eletrotécnica, Campus da Caparica, 2829-516 Caparica, Portugal;

3. CTS-UNINOVA, Campus da Caparica, 2829-516 Caparica, Portugal.

(*) E-mail: pj.lourenco@campus.fct.unl.pt

Received: 21/07/2020 Accepted: 24/09/2020
DOI: 10.7149/OPA.53.3.51042

ABSTRACT:

Over the last decades, the lithographic technology has greatly contributed for the confirmation of Moore's law in the semiconductor industry. Key developments in lithography such as the operational wavelength decreasing, together with a performance increase in lens and imaging technology, enabled the reduction of cost per function in integrated circuits technology. In this work, the impact of lithographic defects introduced by the manufacturing process is analyzed through simulations and two mitigation techniques are presented. These perturbations are a consequence of the limited lithographic mask resolution reflected on deviations from the geometry of the ideal device. For this purpose, the Beam Propagation and Finite Differences Time Domain methods have been used to simulate a multi-mode interference structure based on silicon nitride. The structure is affected by random perturbations and the obtained results revealed a strong dependence between mask resolution, and imbalance and power loss. Two strategies have been followed concerning the mitigation of power loss and imbalance: - Access waveguides tapering and adjustable power splitting ratios through the electro-optic effect. Both strategies revealed results that indicate an improvement on device's performance. However, once built, the former is a static design that favors indiscriminately all propagating modes in the multimode section. In the latter, finer tuning capabilities targeting different propagating modes may be enabled by dynamic compensation of power loss and imbalance, when in a closed loop control architecture. Such a control architecture may operate by sampling the output waveguides, extracting the error signal and, finally, negatively feeding it back to the electro-optic effect system, hence improving imbalance and power loss.

Key words: Beam propagation method, finite differences time domain, multimode interference, lithographic resolution, graphene, chemical potential.

REFERENCES AND LINKS

[1] L. R. Harriott, "Limits of lithography," Proc. IEEE, vol. 89, no. 3, pp. 366-374, 2001.

[2] M. Watanabe, "Active Matrix Driving and Circuit Simulation," in Features of Liquid Crystal Display Materials and Processes, N. K. Kamanina, Ed. InTech, 2011.

[3] N. Yamauchi, Y. Inaba, and M. Okamura, "An integrated photodetector-amplifier using a-Si p-i-n photodiodes and poly-Si thin-film transistors," IEEE Photonics Technol. Lett., vol. 5, no. 3, pp. 319-321, Mar. 1993.

[4] R. Takei, "Amorphous Silicon Photonics," in Crystalline and Non-crystalline Solids, P. Mandacci, Ed. InTech, 2016, p. 21.

 © Sociedad Española de Óptica

[5] S. K. Selvaraja et al., "Low-loss amorphous silicon-on-insulator technology for photonic integrated circuitry," Opt. Commun., vol. 282, no. 9, pp. 1767-1770, 2009.

[6] M. J. Weber, Handbook of Optical Materials, vol. 20, no. 5. CRC Press, 2018.

[7] P. Lourenço, A. Fantoni, and M. Vieira, "Simulation analysis of a thin film semiconductor MMI 3dB splitter operating in the visible range," in Fourth International Conference on Applications of Optics and Photonics, Oct. 2019, p. 4.

[8] P. Lourenço, A. Fantoni, J. Costa, and M. Vieira, "Lithographic mask defects analysis on an MMI 3 dB splitter," Photonics, vol. 6, no. 4, pp. 1-8, 2019.

[9] L. B. Soldano and E. C. M. Pennings, "Optical multi-mode interference devices based on self-imaging: principles and applications," J. Light. Technol., vol. 13, no. 4, pp. 615-627, Apr. 1995.

[10] G. Lifante, Integrated Photonics: Fundamentals. Chichester, UK: John Wiley & Sons, Ltd, 2003.

[11] M. T. Hill, X. J. M. Leijtens, G. D. Khoe, and M. K. Smit, "Optimizing imbalance and loss in 2 x 2 3-db multimode interference couplers via access waveguide width," J. Light. Technol., vol. 21, no. 10, pp. 2305-2313, Oct. 2003.

[12] A. A. Balandin et al., "Superior thermal conductivity of single-layer graphene," Nano Lett., vol. 8, no. 3, pp. 902-907, 2008.

[13] F. Bonaccorso, Z. Sun, T. Hasan, and A. C. Ferrari, "Graphene photonics and optoelectronics," Nat. Photonics, vol. 4, no. 9, pp. 611-622, 2010.

[14] F. Wang et al., "Gate-variable optical transitions in graphene," Science (80-.)., vol. 320, no. 5873, pp. 206-209, 2008.

[15] Z. Lu and W. Zhao, "Nanoscale electro-optic modulators based on graphene-slot waveguides," J. Opt. Soc. Am. B, vol. 29, no. 6, p. 1490, Jun. 2012.

[16] M. Silveirinha and N. Engheta, "Tunneling of electromagnetic energy through subwavelength channels and bends using ε-near-zero materials," Phys. Rev. Lett., vol. 97, no. 15, 2006.

[17] R. Liu et al., "Experimental demonstration of electromagnetic tunneling through an epsilon-near-zero metamaterial at microwave frequencies," Phys. Rev. Lett., vol. 100, no. 2, pp. 1-4, 2008.

[18] R. Sun et al., "Transparent amorphous silicon channel waveguides with silicon nitride intercladding layer," Appl. Phys. Lett., vol. 94, no. 14, 2009.

[19] "Synopsys RSoft Solutions." (accessed Jul. 02, 2020).

1. Introduction

The remarkable success of lithographic technology in semiconductor industry, has persuaded the transference and adaptation of this technology to device manufacturing in the Photonic Integrated Circuit (PIC) industry. However, optical devices present a much higher sensitivity to lithographic imperfections, when compared to the electronic counterparts. This greater reactiveness to imperfections is explained, mainly, by the wavelength at which such devices operate, being similar to the wavelength used for mask transfer [1],

$$Resolution = k_1 \frac{\lambda}{NA}, \qquad (1)$$

where k_1 is a constant that depends on the used process (for integrated circuits manufacturing, k_1 varies from 0.5 to 0.8) and NA is the numerical aperture of the optical lithographic tool (usually NA varies from 0.5 to 0.6).

Only selected few manufacturers have access to state-of-the-art foundries, where resolutions of 100 nm or less are a reality. In most facilities that are able to fabricate such structures, namely research institutes and universities, lithographic mask defects present a performance constraint that must be better understood and mitigated.

On the other hand, hydrogenated amorphous silicon has been extensively used in many real life applications, from thin film transistors in advanced displays to photodetectors [2,3]. This material has also

 © Sociedad Española de Óptica

been considered a reliable platform candidate for the fabrication of PICs. There has been reports in the literature from interconnect waveguides to functional devices, based on this technology [4].

The interest in using this material is mainly explained by its deposition being possible at low temperatures through Plasma Enhanced Chemical Vapour Deposition (PECVD), which makes it back-end compatible with Complementary Metal Oxide Semiconductor (CMOS) manufacturing processes [5]. Moreover, when deposited over silicon dioxide, the created structures present high refractive index contrast, which permits the development of submicron cross section waveguides, with the possibility of describing very small radius bends and, consequently, leading to very high circuit density integration. However, the high spectral absorption of hydrogenated amorphous silicon is located within the visible range, being more transparent at longer wavelengths [4].

This work is part of a wider project, consisting on the development of a biomedical plasmonic sensor. The device functionality is based on the coupling of propagating modes in a dielectric waveguide and the surface plasmon resonance generated on the overlaid metallic layer. This sensor may be fabricated to exploit the high absorption of a-Si:H in the visible spectrum range, if the operating wavelength is located within this part of the spectrum and the detection outcome readout is accomplished by an a-Si:H based photodetector.

To fulfil the requirement of transparency in the visible range for the rest of the structure, silicon compounds may be synthesized. Such is the case of silicon nitride (Si_3N_4) that presents a substantially low extinction coefficient for electromagnetic (EM) energies within the range $380 - 780\ nm$ (visible spectrum) and beyond [6].

Also, the present work materializes as a natural extension of previous research [7,8] where perturbations, introduced along the edges of a Multimode Interference (MMI) device by fabrication processes, are simulated and their influence in the overall performance of the structure is evaluated. Moreover, the latter work [8] reports a statistical analysis of the impact of lithographic mask defects, when considering the manufacturing of a batch of samples and where each sample is affected by an independent random distribution of defects.

2. Methods

2.a. The Multimode Interference 3 dB coupler

The simulated structure is depicted in **Error! Reference source not found.**. It consists on an input waveguide, the middle section which is wide enough to support the MMI phenomenon and two output waveguides. The semiconductor used for the wave-guiding structure is Si_3N_4, for this material transparency is within the visible range. The height/width of both input and output waveguides were selected to assure single mode operation and the input field consisted on the Transverse Electric (TE - 3D) fundamental mode.

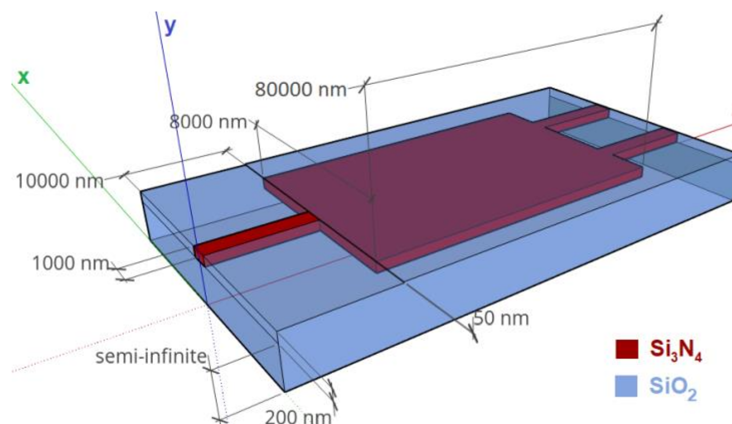

Figure 1 - Generic 1x2 MMI structure geometry and dimensions.

MMI devices rely on the self-imaging principle which states that single or multiple images, of a given input field profile, are replicated periodically in space, as the electromagnetic field propagates through the

 © Sociedad Española de Óptica

waveguide [9,10]. The propagation constant of a mode β_m ($m = 1,2,3,\ldots$), propagating in a high contrast step index multimode device, shows an approximate quadratic dependence to the mode number m:

$$\beta_m \cong k_0 n_{eff} - \frac{(m+1)^2 \pi \lambda_0}{4 n_{eff} W_{eff}^2}, \tag{2}$$

where k_0 is the vacuum wavenumber, n_{eff} the effective refractive index of the structure, λ_0 the vacuum wavelength, and W_{eff} the effective width of the MMI waveguide. The effective refractive index, n_{eff}, is a characteristic of each propagating mode, representing the "experienced" refractive index, when propagating inside the waveguide structure and the standing-wave condition is matched [10]. Hence, the n_{eff} of a given propagating mode may be calculated as in Eq. 3 below:

$$n_{eff} = n_{core} \sin \theta_p , \tag{3}$$

where n_{core} is the core media refractive index, and θ_p is the refraction angle of the transmitted field with respect to the normal at the input interface and at the point of reflection.

The effective width, W_{eff}, is the width when considering the mode field profile penetration depth, due to the Goos-Hähnchen shifts, into the waveguide boundaries. This dimension is polarization dependent and in high refractive index contrast devices, the penetration depth of the EM field beyond the inner walls of the device is practically non-existent, hence W_{eff} can be approximated by the effective width of the fundamental mode [9]:

$$W_{eff} \cong W_{m_0} . \tag{4}$$

The spatial location of single/multiple and direct/mirrored images, resulting from the propagation modes interference, is directly related to the beat length (L_π) of the two lowest order modes:

$$L_\pi = \frac{\pi}{\beta_0 - \beta_1} \cong \frac{4 n_{eff} W_{eff}^2}{3\lambda_0} \cong \frac{4 n_{eff} W_{m_0}^2}{3\lambda_0} . \tag{5}$$

Single mirrored and direct images from the input field profile form at $3L_\pi$ and $2(3L_\pi)$, respectively, while two-fold images form at $\frac{1}{2}(3L_\pi)$ and $\frac{3}{2}(3L_\pi)$. Single images are, approximately, the same amplitude as the input EM field and each of the two-fold images is affected by a 3 dB attenuation factor, thus offering the ideal conditions for a power splitter device, similar to the structure diagram depicted in **Error! Reference source not found.**. This schematic represents a Si_3N_4 MMI device embedded in SiO_2 and associated dimensions, which were used throughout this paper in our simulations and subsequent analysis.

Moreover, by using an interference mechanism designated as symmetric interference, $1 \times N$ power splitters may be designed with quarter-length MMI sections. The mechanism relies on preventing the excitation of odd order modes within the multimode section of the structure. This is attained by placing the input waveguide, with a propagating symmetric field profile (e.g., Gaussian beam), at the width centre of the MMI section, thus resulting in N linear combinations of the input profile located at:

$$L = \frac{p}{N}\left(\frac{3L_\pi}{a}\right), \tag{6}$$

where $p \geq 0, N \geq 1, p$ and N are integers, have no common divisor and $p/_N$ represents $1^{st}, 2^{nd}, \ldots, n^{th}$ single and N-fold images at location L; a denotes the type of coupler (for an $1 \times N$ power splitter, $a = 4$).

According to the literature [11], excess loss and imbalance between the output waveguides are two of the most influent characteristics on a 3 dB MMI coupler, when considering its performance. These constraints are due to deviations from the geometry of the ideal device, introduced by fabrication tolerances. Imbalance

 © Sociedad Española de Óptica

is particularly disadvantageous in our case. Being this research part of a broader project that intends to develop a biomedical plasmonic sensor and where there will be a reference and a sensing arms, power imbalance between the outputs will result in a reduction of sensing capabilities.

This work will take into consideration two approaches to mitigate the impact of the main causes of excess loss and power imbalance in these devices, namely the lithographic mask limited resolution:

- The insertion of tapers to adapt the width mismatch between the access waveguides and the wider MMI section;
- By using graphene sandwiched between dielectric waveguides and placed at strategic locations along the MMI structure to control the influence of propagating modes inside the multimode section.

2.b. Background

Graphene has been a subject of intense research for some years now, because of its remarkable electronic and optical properties. It presents flexibility, robustness, environmental stability [12] and singular optical properties, such as, strong light coupling [13] and optical conductivity controlled by bias gating [14]. This gate variable optical conductivity is of high interest for electro-optical (EO) modulation.

According to Lu et al. [15], there are two absorption processes in light-graphene interaction. These processes are the inter-band and intra-band absorptions, which together characterize the complex conductivity of graphene:

$$\sigma_t = \sigma_{intra}(\omega, \mu_c, \Gamma, \mathrm{T}) + \sigma_{inter}(\omega, \mu_c, \Gamma, \mathrm{T}) \,, \qquad (7)$$

where, ω is the light angular frequency, μ_c is the chemical potential, Γ is the charged particle scattering rate and T is the temperature. Because the chemical potential may be electrically controlled, the conductivity of graphene can be tuned through gating voltage V_f.

In this work, we evaluated the evolution of the permittivity of graphene with the chemical potential, at the wavelength of operation for our MMI structure (650 nm), to determine if this feature of graphene could also be exploited at this wavelength. **Error! Reference source not found.** presents the behaviour of graphene for our particular case.

As can be observed in the above figure, at the operating wavelength of 650 nm, when the chemical potential reaches 1,325 eV and above, the real part of graphene permittivity crosses zero while the imaginary part remains constant. This corresponds to a sign inversion of the real part of permittivity and is usually associated to a resonance often described as the ``near-zero-epsilon". Such effect is not a particularity of graphene, for many other materials [16,17] also possess a plasma frequency which is characterized by a metallic-like behaviour, only in graphene this resonance may be reached through electrical gating.

 © Sociedad Española de Óptica

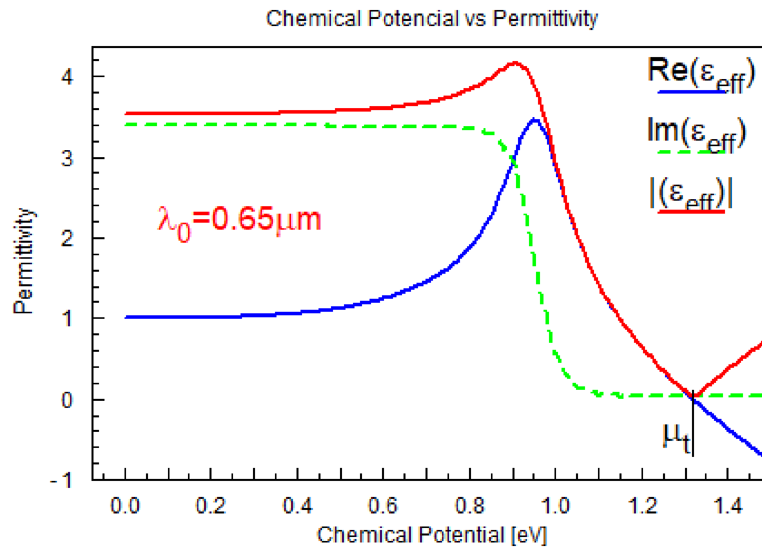

Figure 2 - Permittivity of graphene with the chemical potential when free space wavelength is 650nm.

3. Simulations

In previous work [7,8], we assessed through numerical simulations the width offset from the ideal geometry of the MMI device, which is introduced by manufacturing processes. In this paper, we keep the same approach regarding the structure design conditions. The simulated structure consists of input and output waveguides, and the MMI section, affected by independent defects distributions along their longitudinal edges.

Defects distribution standard deviation influences the width (X-axis) of all structure sections, along the propagation length (Z-axis), and are independent in each section of the structure (input and output waveguides, and MMI section). It was assured that defects on the left and right longitudinal edges of each section were not correlated to one another, nor even within sections. The correlation length of the random distributions of defects was selected as the full length of each section (access waveguides and multimode sections), to properly emulate real-world distribution of perturbations.

A silicon nitride waveguide buried in silicon dioxide is not a usual waveguide design. However, there are some reports in the literature which have implemented similar technology. Namely, for the manufacturing of such a device, the process could rely on a bottom thermal SiO_2 substrate, followed by Plasma Enhanced Chemical Vapor Deposition (PECVD) of the Si_3N_4 waveguide and an SiO_2 cladding, which can be obtained by a PECVD process [18] or by plasma gas decomposition [4].

3.1. Access waveguides taper

At this stage, our work considered the evaluation of the impact of inserting linear tapers in each access waveguide. Through RSoft [19] software suite platform, a set of simulations were carried out on a device with dimensions as listed in Table 1. The MMI section length was determined considering equation 6, with corresponding parameters for a 3 dB power splitter device (p = 1, N = 2 and a = 4).

Table 1 - Waveguides and multimode sections dimensions.

Section	*width* [μm]	*height* [μm]	*length* [μm]
waveguide	1	0.2	10
multimode	8	0.2	90.4

The schematic presented in Figure 3 reflects the impact of the random distribution of defects along the longitudinal edges of the simulated structure, where the whole device is embedded in SiO_2 with a 50 nm cover layer and the superstrate is air.

 © Sociedad Española de Óptica

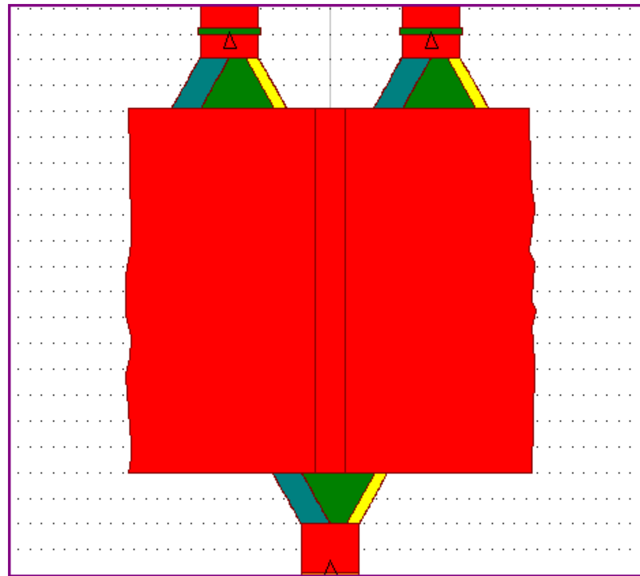

Figure 3 - Simulation workspace of the tapered MMI structure.

Next, we defined the power imbalance between the output waveguides as the ratio represented by equation 8:

$$Imbalance = \frac{Out_2 - Out_1}{Out_2 + Out_1}, \quad (8)$$

Simulations were conducted considering the operating wavelength $\lambda = 650\ nm$, the TE fundamental mode as the input field and 10 nm standard deviation for the random distribution of defects, while iterating the width of the linear tapers located between the multimode section and the access waveguides. By monitoring the power at the end of the output waveguides, we were able to obtain the results presented in Figure 4.

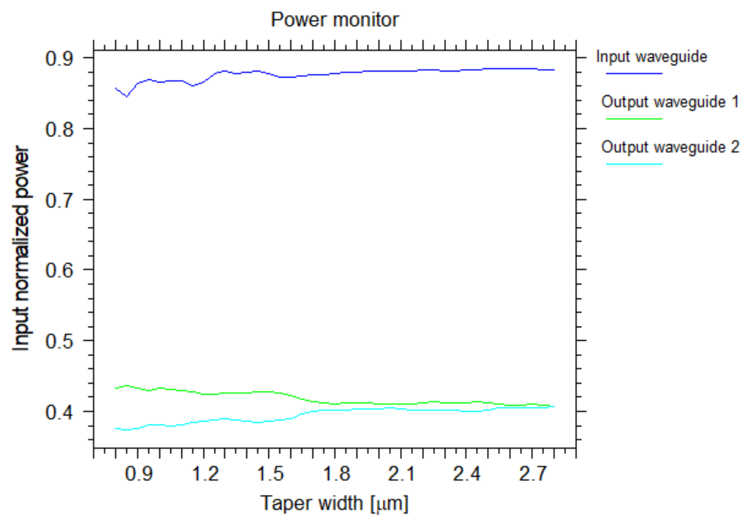

Figure 4 - Power imbalance and insertion loss vs taper width for 10nm standard deviation of a random distribution of defects.

Previous mentioned figure clearly shows that, as the taper width increases, the field intensity at both the output waveguides converges, hence minimizing power imbalance. Consequently, insertion loss also decreases which is denoted by a slight increase on the monitored input power. These results seem to be in accordance with the work presented in Hill et. al [11], which states that the ratio between the optimal access waveguide and the multimode section widths should be approximately 0,3.

3.2. Dynamic tuning

 © Sociedad Española de Óptica

As stated before in this paper, optical conductivity of graphene may be controlled by bias gating. We propose that, by placing layers of graphene at strategic locations, namely where direct/mirrored images of the input profile are formed within the MMI section, we might be able to control independently the influence of a given image or images, on the corresponding affected output. If this control bias depends on the output power verified in one of the exiting waveguides then, by negative/positive feedback, we might be able to dynamically tune the imbalance verified between output waveguides.

Figure 5 presents an MMI structure, where the propagating field is controlled by the bias applied on the graphene layer. By varying the chemical potential of graphene, one is able to affect its resonance at a given wavelength, hence the propagating field intensity may be modulated through bias gating of graphene.

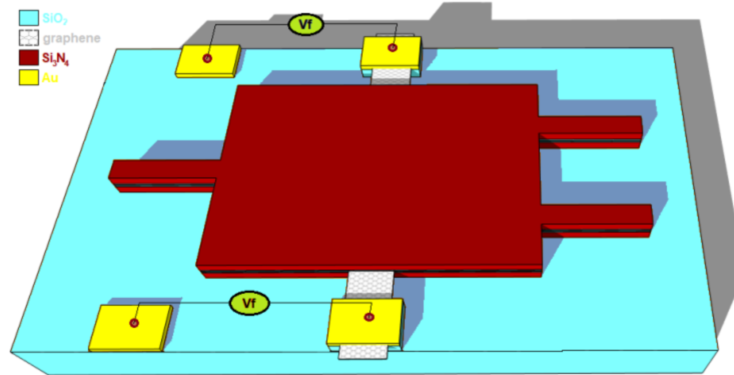

Figure 5 - Schematic of MMI structure with control through bias gating of graphene.

Based on Figure 2 and the results presented regarding the change on the dielectric constant with increasing chemical potential, we used a mode solver to determine the modal index of the TE fundamental mode on a multilayer waveguide 2 μm wide and with the layers composition as presented in Table 2:

Table 2 - Multilayer structure composition and individual layers heights.

Dielectric	Layer height
Si_3N_4	90 nm
SiO_2	10 nm
$Graphene$	0.7 nm
SiO_2	10 nm
Si_3N_4	90 nm

Our intent was to evaluate the impact of the chemical potential μ_c variation on the propagating modes. We also considered SiO_2 as the substrate and air for the cladding. Figure 6a) represents the transverse refractive index profile of the waveguide utilized by the mode solver to determine the TE fundamental mode supported by the multilayer waveguide. Figure 6b) shows the fundamental mode profiles when the chemical potential of graphene is 0 eV (top) and 1,325 eV (bottom). Note the difference between the imaginary parts of the modal indices present at the top and bottom profiles. The bottom profile presents a value over two orders of magnitude lower and the same behaviour has been verified in the first 4 modes (four propagating modes were searched with the mode solver, although this structure supports higher order modes).

The complex value of the modal index of a given mode is defined as in equation 9:

$$n_{eff} = n + ik \, , \tag{9}$$

where, n and k correspond to the real and the imaginary parts, respectively, of complex value n_{eff}; k is often referred to as the extinction coefficient and is directly related to the absorption of the material, as in equation 10:

$$\alpha = {}^{4\pi k}/_{\lambda} \, , \tag{10}$$

 © Sociedad Española de Óptica

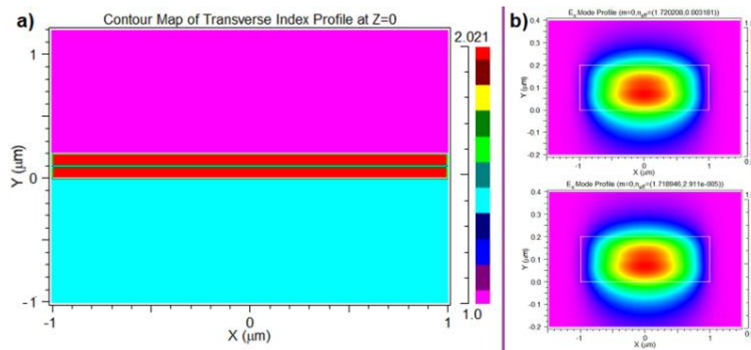

Figure 6 - a) Transverse refractive index profile of simulated waveguide; **b) [top]** fundamental mode profile when $\mu_c = 0\ eV$ and **b) [bottom]** fundamental mode profile when $\mu_c = 1,325\ eV$.

where α and k, are respectively, the absorption and extinction coefficients, and λ is the free space wavelength. By evaluating the attenuation corresponding to the two chemical potential situations, we are able to calculate loss as approximately 0,3 $dB\mu m^{-1}$ and 0,002 $dB\mu m^{-1}$, respectively for $\mu_c = 0\ eV$ and $\mu_c = 1{,}325\ eV$.

Furthermore, and to properly evaluate the whole MMI structure and its behavior when subjected to EM field radiation, we had to configure our simulation tools [19] accordingly. One must remember that the MMI device is too long to be simulated by the Finite Differences Time Domain (FDTD) algorithm and that the Beam Propagation method is not accurate enough to simulate a graphene layer 0,7 nm high. Certainly, FDTD can perform a simulation over the entire 3D structure and, simultaneously, being able to "see" the 0,7 nm high graphene layer, only not within sensible limits of time.

Also, this time we considered an MMI structure (similar to the one presented in Figure 5) 8 μm wide, 108 μm long in total (88 μm for the MMI section and 10 μm for each input and output waveguides) and 200,7 nm thick (0.7 nm accounts for graphene thickness). This is an Si_3N_4 structure deposited on an SiO_2 substrate and where are also deployed the metallic contacts. Beneath this substrate there should be a metallic plane to assure enough charge carriers for the development of an electric field on the above placed graphene layer and, at the same time, to avoid collisions between these charge carriers and the incoming photons of the propagating EM field.

Hence, for previously mentioned above reasons, our simulation domain had to be divided in three sections, from the input waveguide up to 52 μm (1 μm before the graphene section), from 52 μm to 56 μm (1 μm after the graphene section) and from 56 μm to the end of simulation domain. Each section was handled by the appropriate software tool and the outcome results were passed over to the next simulation stage tool. The tool sequence followed is shown in Table 3, together with the simulated propagation length and the intended outcome of each step:

Table 3 - Simulation lengths and tools sequence.

Algorithm	Length	Objective
1. Mode solver	10 μm	Obtain input field
2. BPM	52 μm	Obtain end field
3. FDTD	4 μm	Obtain end field
4. BPM	52 μm	Propagate to the end

The FDTD simulations were executed on the central section of the structure, where the graphene multilayer structure extends from 53 μm to 55 μm. Figure 7 and Figure 8 depict a Z-cut ($z = 54\ \mu m$) view of this structure refractive index, considering both chemical potential levels for graphene, $\mu_c = 0\ eV$ and $\mu_c = 1{,}325\ eV$. The outsets show a one-dimensional vertical cut of the refractive indices and their distribution through the area where graphene has been deposited. These images enable the visualization of the chemical potential impact on graphene's refractive index with each μ_c selected level. As may be observed, when the chemical potential is $\mu_c = 1{,}325\ eV$, the real part of the refractive index of graphene is close to zero (see the outset of Figure 8, corresponding to the material "near-zero-epsilon" resonance presented in Figure 2 and which characterizes a "metallic-like" behavior of graphene.

 © Sociedad Española de Óptica

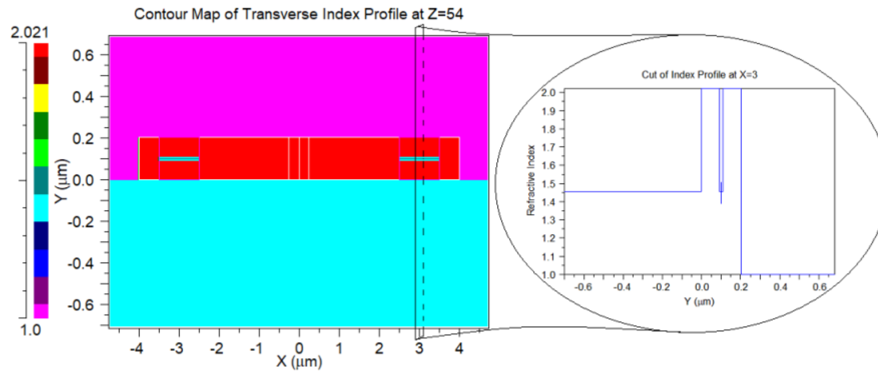

Figure 7 - Z-cut of the structure where graphene is located; the outset represents a vertical cut showing the impact of chemical potential ($\boldsymbol{\mu_c = 0\ eV}$) on the refractive index of this structure.

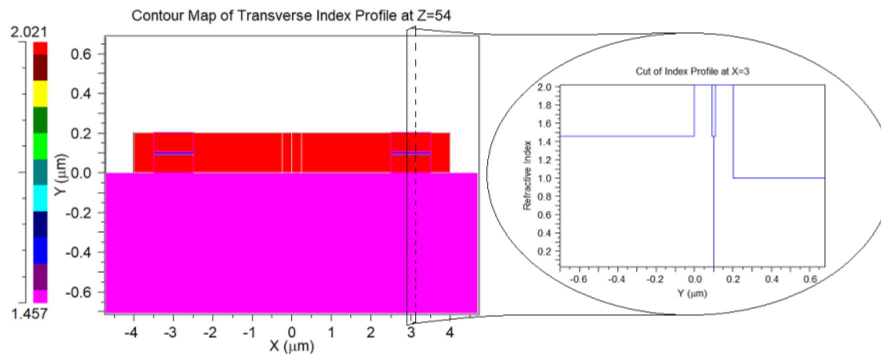

Figure 8 - Z-cut of the structure where graphene is located; the outset represents a vertical cut showing the impact of chemical potential ($\boldsymbol{\mu_c = 1,325\ eV}$) on the refractive index of this structure.

Next follows the results obtained by FDTD simulation, presented in Figure 9, at the end of the graphene section and for both values of chemical potential. One is able to notice the amplitude difference verified between the two Poynting vector profiles, namely near the x-axis edges of the simulation domain (Figure 9b). These results were obtained by varying on both graphene layers the chemical potential (either $\boldsymbol{\mu_c = 1,325\ eV}$ or $\boldsymbol{\mu_c = 0\ eV}$), which emulates a gating voltage V_f variation (see Figure 5) and corresponding deformation of the Fermi level of graphene.

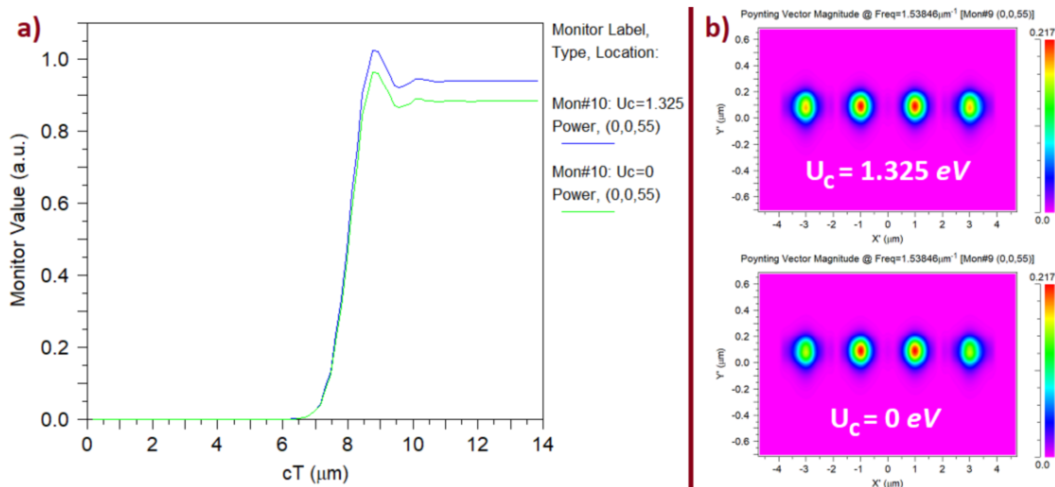

Figure 9 – a) Normalized power at the end of graphene section when $\boldsymbol{\mu_c = 1,325\ eV}$ and $\boldsymbol{\mu_c = 0\ eV}$; **b)** Poynting vector magnitude at the end of graphene section for $\boldsymbol{\mu_c = 1,325\ eV}$ (top) and $\boldsymbol{\mu_c = 0\ eV}$ (bottom).

Finally, follows the simulation of the rest of the structure. Again, the beam propagation method has been used to simulate this last section and Figure 9 shows the results obtained on both output waveguides for both chemical potential cases, $\mu_c = 1{,}325\ eV$ and $\mu_c = 0\ eV$. The observed difference between the two distinct μ_c instances is not of great significance, but one must not forget that the power difference previously observed at the end of the graphene layers has been diluted through interference in the rest of the multimode section. Moreover, this corresponds to 2 μm long and 1 μm wide graphene layers, and that the

 © Sociedad Española de Óptica

same chemical potential has been assumed for both of these layers at each simulated instance, which would not be the case if we were to compensate the power imbalance between the output waveguides in a closed loop dynamic control. In that case, it would be assumed a chemical potential differential between both graphene layers, resulting from the negative/positive feedback given by the dynamic closed loop control.

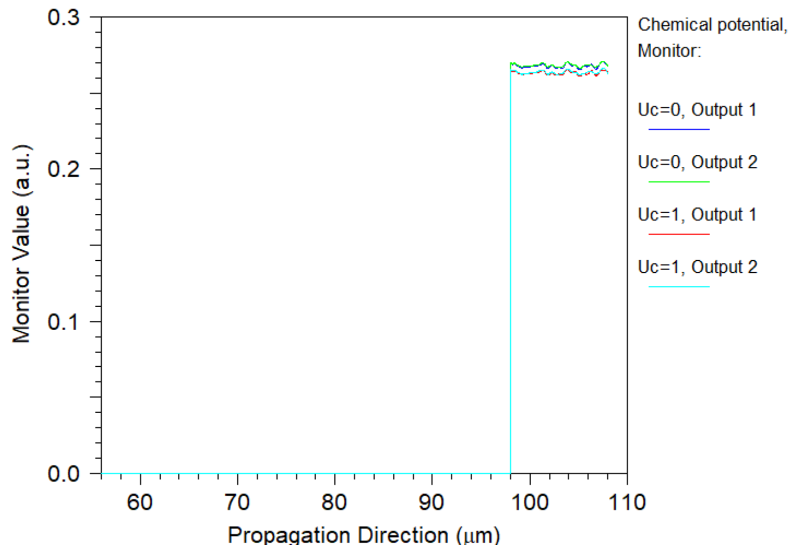

Figure 10 - Normalized power at the output waveguides for both chemical potential instances ($\boldsymbol{\mu_c = 1,325\ eV}$ and $\boldsymbol{\mu_c = 0\ eV}$).

4. Conclusions

Lithographic resolution presents a serious constraint on MMI devices performance. In this work and through simulation, we have presented and proposed two different strategies to mitigate the impact of limited lithographic mask resolution. The approach where tapered access waveguides were simulated, has revealed that the power imbalance between the output waveguides and insertion loss can be both minimized by using linear tapers with specific width. This work is in accordance with analytical predictions calculated by Hill et al. [11] and where it is stated that there is an optimal ratio between the multimode section and the tapers widths.

In our second approach, we propose a dynamic control of the optical conductivity of graphene through electrical gating. By adjusting the EM field amplitude in precise locations within the multimode section, we should be able to minimize the power imbalance at the output waveguides. This could be achieved through a negative/positive feedback system that monitors the power at each output waveguide and controls the gating bias that is applied to graphene. For instance, by sampling the outputs of the device, extracting the error between them and then, negatively feeding it back into the electro-optic effect system, in a closed loop control architecture of the electrical gating. Our simulations showed that, by biasing graphene, the attenuation of the EM field amplitude can have a variation of over two orders of magnitude, which offers good prospects for power imbalance reduction.

Further work will consist in also evaluating the impact of graphene gating on the phase of the EM field and its possible applications, and on optimizing the multilayer structure by conducting simulations with different semiconductors.

Acknowledgements

This work is an extended version of the article https://doi.org/10.1117/12.2555564} presented at SPIE Photonics Europe 2020 and published in the Conference Proceedings Volume 11364, Integrated Photonics Platforms: Fundamental Research, Manufacturing and Applications; 113641Q (2020).

It has also been supported by EU funds through the LISBOA-01-0145-FEDER-031311 European Regional Development Fund and by Portuguese national funds provided by FCT – Fundação para a Ciência e a Tecnologia through grant SFRH/BD/144833/2019 and projects PTDC/NAN-OPT/31311/2017 and UID/EEA/00066/2020, and by projects IPL/2019/BioPlas-ISEL and IPL/2019/MO-TFT-ISEL.

 © Sociedad Española de Óptica